

Problem-informed Graphical Quantum Generative Learning

Bence Bakó,^{1,2} Dániel T. R. Nagy,^{1,2} Péter Hágá,³ Zsófia Kallus,³ and Zoltán Zimborás^{1,2,4,5}

¹*Eötvös Loránd University, Budapest, Hungary*

²*HUN-REN Wigner Research Centre for Physics, Budapest, Hungary*

³*Ericsson Research, Budapest, Hungary*

⁴*Algoirthmique Ltd, Kanavakatu 3C, Helsinki, 00160, Finland*

⁵*QTF Centre of Excellence, Department of Physics, University of Helsinki, Helsinki, Finland*

Leveraging the intrinsic probabilistic nature of quantum systems, generative quantum machine learning (QML) offers the potential to outperform classical learning models. Current generative QML algorithms mostly rely on general-purpose models that, while being very expressive, face several training challenges. One potential way to address these setbacks is by constructing problem-informed models that are capable of more efficient training on structured problems. In particular, probabilistic graphical models provide a flexible framework for representing structure in generative learning problems and can thus be exploited to incorporate inductive bias into QML algorithms. In this work, we propose a problem-informed quantum circuit Born machine Ansatz for learning the joint probability distribution of random variables, with independence relations efficiently represented by a Markov network (MN). We further demonstrate the applicability of the MN framework in constructing generative learning benchmarks and compare our model's performance to previous designs, showing that it outperforms problem-agnostic circuits. Based on a preliminary analysis of trainability, we narrow down the class of MNs to those exhibiting favourable trainability properties. Finally, we discuss the potential of our model to offer quantum advantage in the context of generative learning.

I. INTRODUCTION

In recent years, the field of machine learning (ML) experienced unprecedented growth, giving rise to a wide variety of models and algorithms with the potential to revolutionize several fields [1]. Generative learning is a powerful paradigm in ML that aims to capture the underlying distribution of data in order to generate realistic samples [2]. Quantum machine learning (QML) has emerged as a promising intersection of quantum computing and machine learning in the pursuit of practical quantum advantage [3, 4].

Quantum resources, due to their inherent probabilistic nature, can be used to efficiently draw samples from probability distributions of high complexity [5–9]. This makes generative QML a natural pathway towards harnessing the potential of quantum computers. Recent advances in this field led to the adaptation of several successful classical generative models [10]. The resulting architectures include quantum circuit Born machines (QCBMs) [11–13], quantum generative adversarial networks (QGANs) [14, 15] and quantum Boltzmann machines (QBM) [16, 17].

While their high expressivity makes general-purpose QML models very powerful, they also pose several challenges. Contrary to classical neural networks, variational quantum circuits are much more affected by trainability issues, such as barren plateaus and poor local minima [18–22]. Furthermore, the no-free-lunch theorem [23] also translates to QML, suggesting, that these problem-agnostic models, like hardware-efficient Ansätze, have poor average performance [24, 25]. The reason behind these barriers can be seen as the lack of sufficient inductive bias, i.e., assumptions about the data

that could be encoded into the learning framework. Consequently, a potential way of dealing with them is by constructing problem-informed models, that can be trained more efficiently for structured problems [26–30].

Probabilistic graphical models (PGMs) provide a mathematical framework for representing structure in generative learning problems defined over random variables [31] and, as such, can be exploited to construct problem-informed QML models, as depicted in Fig. 1. The two main classes of PGMs are Bayesian networks (BNs) and Markov networks (MNs). BNs provide a highly interpretable approach to graphical modelling by using a directed graph, leading to numerous real-world applications across many disciplines [32]. However, in certain domains, such as those involving spacial or relational data, MNs provide a more natural representation, since they do not define the orientation of the graph edges [33].

While there are several excellent works concerning the quantum circuit implementation of BNs [34–36], MNs are not well-studied in the context of QML. In this work, we investigate the applicability of the framework provided by MNs to generative QML with classical data. We propose a problem-informed model, that aims to learn the distribution over random variables, where the independence relations are efficiently represented by a MN. As opposed to previous problem-agnostic QCBMs, this Ansatz can capture higher-order correlations between the corresponding random variables and potentially reduce the number of trainable parameters, while also increasing performance. Throughout the paper, by higher-order correlations, we refer to correlations, that cannot be described by fewer-body (e.g., pairwise) relationships. While this construction relies on the knowledge of the

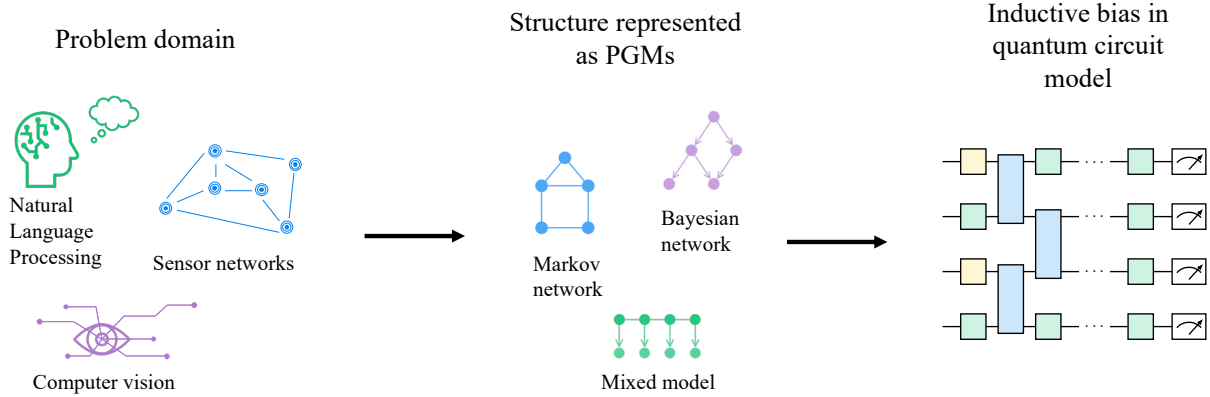


FIG. 1. **Framework for using probabilistic graphical models to introduce inductive bias in quantum generative learning models.** Most generative learning problems can be (re)formulated with binary random variables. If we have enough knowledge about the problem, we can identify structure in the form of PGMs. Having a PGM, we can construct and train the corresponding quantum model, that later can be used to draw samples from the learned probability distribution.

MN structure, that can be hard to infer from data, the graph representation is readily available in various application domains. We argue that this new model class has the potential to demonstrate quantum advantage, since it contains the class of QAOA circuits [37], that were shown to produce classically hard probability distributions [7, 38]. Besides model design, we also show the potential of the PGM framework to construct benchmarks for generative QML models, where the problem complexity can be fine-tuned in multiple factors. We perform numerical experiments based on this benchmark proposal against both problem-agnostic and BN-based QML models. Finally, we present a preliminary analysis of trainability and define a class of efficient graphical representations, that have higher potential in this context.

It is important to note that, while we concentrate on the significance of problem-specific model construction in the context of QML, this trend is also present in classical ML, where much larger models can be implemented [39]. This further illustrates the power of problem-informed approaches, relevant not only for near-term devices, but potentially for the large-scale fault-tolerant quantum computing as well.

The structure of this paper is as follows: Sec. II offers a review of relevant concepts regarding PGMs and generative QML. In Sec. III, we present our generative QML model and benchmark proposal, along with numerical experiments. Finally, in Sec. IV, we discuss potential future directions.

II. BACKGROUND & NOTATION

A. Probabilistic Graphical Modelling

Explicitly encoding the probabilities of each assignment in a high-dimensional state-space is infeasible,

as it scales exponentially with the number of random variables. In a space of only ten binary variables, we would need $2^{10} = 1024$ numbers to represent a probability distribution. PGMs were developed to tackle this problem by using a graph representation to compactly encode a complex distribution of interacting random variables. These graphs effectively capture the independence relations between variables and enable to split the joint probability distribution into smaller factors, each over a smaller subspace. Furthermore, this framework is also useful for inference and learning tasks.

Here we give a brief description of the mathematical framework of the two main families of PGMs and their connections. Since any higher-order PGM can be embedded into PGMs over binary random variables, we focus our attention on the latter. For an extensive study of PGMs, we refer the reader to Ref. [31].

1. Bayesian networks

BNs use directed acyclic graphs to represent the conditional dependencies between random variables. In these models, a variable is independent of all other variables given its parents in the graph. Consequently, the factors of the joint probability distribution can be interpreted simply as conditional probabilities.

Definition 1 (Bayesian network factorization). *A distribution P_B over the space of n random variables $\mathbf{X} = \{X_1, \dots, X_n\}$ factorizes according to a Bayesian network $\mathcal{B} = (\mathcal{G}, P)$, if P_B can be expressed as a product*

$$P(X_1, \dots, X_n) = \prod_{i=1}^n P(X_i | Pa_{X_i}^{\mathcal{G}}),$$

where $Pa_{X_i}^{\mathcal{G}}$ denotes the parents of the node associated to variable X_i in graph \mathcal{G} .

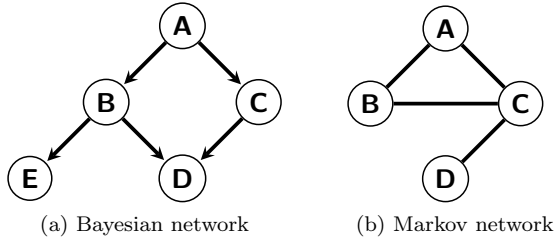


FIG. 2. **Small examples of the two main classes of probabilistic graphical models.** The nodes represent random variables, the edges represent some dependence between them. Bayesian networks have directed edges, denoted by arrows, Markov networks have undirected edges.

As an example, in the BN presented in Fig. 2a, the set of independencies can be written as: $(B \perp C \mid A)$, $(D \perp A \mid B, C)$, $(E \perp C, D \mid B)$. As per Def. 1, the joint probability distribution is $P(A, B, C, D, E) = P(A)P(B|A)P(C|A)P(D|B, C)P(E|B)$.

2. Markov networks

Markov networks, Markov random fields or undirected graphical models are defined over general undirected graphs to represent a set of random variables having the Markov property. In general, the global Markov property applies, which states, that any two subsets of variables are conditionally independent given a separating subset. As opposed to BNs, where the factors are straightforward to comprehend, here they cannot be interpreted directly. However, we can view a factor as describing “compatibilities” between different values of the variables in the corresponding subset. A factor here describes a general purpose function $\phi : \text{Val}(\mathbf{D}) \rightarrow \mathbb{R}$, where $\text{Val}(\mathbf{D})$ denotes all possible joint states of a set of random variables \mathbf{D} . Each factor corresponds to a clique in the graph, however, the usual graphical representation does not make it clear, whether the joint probability distribution only factorizes according to the maximal cliques or also the subsets thereof. However, the maximal clique factorization is the most general for a given graph, therefore, in general, we work with this assumption.

Definition 2 (Markov network factorization). *We say that a distribution P_Φ with $\Phi = \{\phi_1(\mathbf{D}_1), \dots, \phi_K(\mathbf{D}_K)\}$ factorizes over a Markov network \mathcal{H} if each \mathbf{D}_k ($k = 1, \dots, K$) is a complete subgraph of \mathcal{H} and P_Φ is a Gibbs distribution parametrized by these factors as follows:*

$$\begin{aligned} P_\Phi(X_1, \dots, X_N) &= \frac{1}{Z} \tilde{P}_\Phi(X_1, \dots, X_N) \\ &= \frac{1}{Z} \phi_1(\mathbf{D}_1) \times \phi_2(\mathbf{D}_2) \times \dots \times \phi_K(\mathbf{D}_K), \end{aligned}$$

where \times denotes the factor product, \tilde{P}_Φ is the unnormal-

ized measure and

$$Z = \sum_{X_1, \dots, X_n} \tilde{P}_\Phi(X_1, \dots, X_n)$$

is the normalizing constant or partition function.

For the MN in Fig. 2b, with independence relations $(A \perp D \mid C)$, $(B \perp D \mid C)$ and assuming maximal clique factorisation, the joint probability distribution, according to Def. 2, takes the form $P(A, B, C, D) = \frac{1}{Z} \phi_1(A, B, C) \phi_2(C, D)$. Here $\phi_1(A, B, C)$ and $\phi_2(C, D)$ denote the two maximal cliques of the graph.

In this picture, the factors are encoded as complete tables, however, for positive factor values, there exists an alternative parametrization, that connects MNs to energy-based models [40]. In this case, the joint probability distribution can be written as

$$P_\Phi(X_1, \dots, X_N) = \exp \left\{ \left[- \sum_{i=1}^m \epsilon_i(\mathbf{D}_i) \right] \right\}, \quad (1)$$

where $\epsilon_i(\mathbf{D}_i) = -\ln \phi_i(\mathbf{D}_i)$ is called the energy function. This parametrization of MNs is usually referred to as the log-linear model. We use this representation as inspiration for constructing our MN-based QML model.

3. Connection between BNs and MNs

Bayesian and Markov networks are incomparable in terms of independence relations they capture. However, we can convert one type into the other, that can represent the same probability distribution by potentially introducing new edges between the nodes of the graph.

The transformation from BNs to MNs, called moralization, follows a simple rule: if two nodes are connected by a directed edge in the BN graph, or they are both parents of at least one node, then they are connected by an undirected edge in the MN graph. Having the undirected graph, we can assign a factor to each resulting clique, to obtain a MN. This procedure usually leads to a PGM with more parameters, that can lead to a longer training. Directed graphs, in which parent nodes do not share common children, are called moral. Consequently, BNs that are defined over moral graphs, can be converted to MNs without introducing additional edges and parameters.

Turning MNs into BNs is a more difficult task, both conceptually and computationally. First, the undirected graph needs to be triangulated, meaning that we introduce chords in cycles of 4 or more and repeat this process until there are no such cycles left. Chords connect nodes, that are in the cycle, but are not already connected. This transformation usually leads to the introduction of a much larger number of edges than in the previous case. Finally, the undirected edges have to be turned into directed ones in an acyclic manner. Since chordal graphs are also moral, PGMs that are defined

over chordal graphs represent a class of graphical models, that can be treated as either BNs or MNs and the conversion between the two is straightforward.

4. Generative learning in PGMs

The two main learning tasks in the context of PGMs are structure learning and parameter estimation [31]. In this work, we restrict our attention to a version of parameter estimation in a generative learning setting. We require our model to learn how to sample the unknown probability distribution that the corresponding PGM induces. We give a formal description of this problem for MNs, but it can be formulated for BNs analogously to Prob. 1. Throughout this work, we use the phrases distribution learning and generative learning interchangeably.

Problem 1 (Distribution Learning in MNs). *Given the graph structure and the clique factorization of a Markov network \mathcal{H} with an unknown joint probability distribution P^* , a dataset \mathcal{D} sampled from P^* and $\varepsilon, \delta \in (0, 1)$, output with probability at least $1 - \delta$ a representation of a distribution $P_{\mathcal{M}}$ satisfying $d(P^*, P_{\mathcal{M}}) \leq \varepsilon$.*

In the above problem formulation, $d(\cdot, \cdot)$ refers to the distance between the two distributions. In this work, we focus on the total variational (TV) distance defined as

$$\text{TV}(P^*, P_{\mathcal{M}}) = \frac{1}{2} \sum_{x \in \{0,1\}^n} |P^*(x) - P_{\mathcal{M}}(x)|. \quad (2)$$

In MNs, the use of a normalizing constant couples the parameters across the whole network, which prevents us from decomposing the problem and estimating local groups of parameters separately. One of the computational ramifications of this global coupling is, that not even the parameter estimation with complete data can be solved in closed form (except for some special cases, that can essentially be reformulated as BNs [41]). This makes the use of iterative methods, such as gradient descent, unavoidable. Luckily, the objective function is convex, meaning that these methods are guaranteed to converge. However, they come with the disadvantage of having to run inference in each step to calculate the gradients and inference in MNs is #P-complete in general, which makes the distribution learning task formulated above fairly expensive or even intractable classically [42].

B. Generative QML Models

1. General framework of QCBMs

QCBMs, introduced in Ref. [11], are paradigmatic generative QML models, that naturally inherit the Born

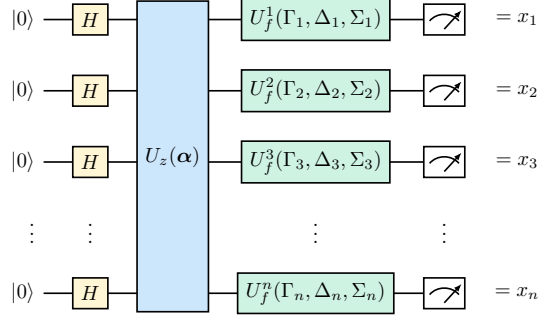


FIG. 3. **General structure of the quantum circuit Ising Born machine, adapted from [13].** The circuit starts with Hadamard gates on each qubit, then a parametrized n -qubit unitary is applied with tunable parameters α , finally, a general parametrized U_f gate acts on each qubit separately. The measurement is taken in the computational basis.

rule and thus can be used to generate tunable and discrete probability distributions that approximate a target distribution. In this section, we review the general components of variational quantum algorithms in the context of QCBMs.

One of the key building blocks is the Ansatz. The Ansatz refers to a parametrized family of quantum circuits used as a hypothesis or approximation for solving the problem in question by iteratively optimizing the parameters to match the desired target behaviour or to minimize a cost function. We can differentiate problem-informed and problem-agnostic Ansätze.

The quantum circuit Ising Born machine (QCIBM), introduced by Coyle et al. in [13], in its most general form, is a problem-agnostic Ansatz. The structure of the QCIBM circuit is depicted in Fig. 3, where the corresponding unitaries can be written as

$$U_z(\alpha) = \prod_j U_z(\alpha_j, S_j) = \prod_j \exp \left\{ \left(i \alpha_j \bigotimes_{k \in S_j} Z_k \right) \right\}, \quad (3)$$

$$U_f(\Gamma, \Delta, \Sigma) = \exp \left\{ \left(i \sum_{k=1}^n (\Gamma_k X_k + \Delta_k Y_k + \Sigma_k Z_k) \right) \right\}. \quad (4)$$

Here each S_j indicates a subset of qubits and the X, Y, Z operators are the Pauli-matrices. The U_f operators can also be thought of as a “parametrized measurement”, or letting the measurements be in any local basis. The authors restrict the Hamiltonian, that generates U_z to only contain one- and two-body terms, since “only single and two-qubit gates are required for universal quantum computation” and they consider each qubit-pair (all-to-all connectivity).

The goal of generative learning is to draw samples from a model probability distribution P_{θ} , that is sufficiently close to the target distribution P^* , while only

having access to a finite number of samples from P^* . In the case of QCBMs, the model probability distribution is approximated by repeatedly running the circuit and measuring an observable each time. The final measurements are performed in the computational basis on each qubit, producing a binary string of variables $x_i \in \{0, 1\}$ from the distribution

$$P_{\theta}(\mathbf{x}) = |\langle \mathbf{x} | U(\theta) | 0 \rangle^{\otimes n}|^2, \quad (5)$$

where the θ vector contains all circuit parameters.

There are multiple ways to characterize the distance of two distributions. The TV distance, shown in (2), is a good benchmark, but it is not feasible as a cost function, as it uses the probabilities explicitly. While in principle, one can use an approximation of the probability distributions based on a finite number of samples, the required number is exponential in general. One of the most common metrics used as a cost function in generative modelling is the Kullback-Leibler (KL) divergence

$$D_{KL}(P_{\theta}, P^*) = \sum_x P^*(x) \log \left(\frac{P^*(x)}{P(x)} \right), \quad (6)$$

where in practice $P(x)$ is replaced by an infinitesimal constant for 0 probabilities.

Unfortunately, this function is also unsuitable for data-driven training, as it requires a large number of training samples, and it was shown not to be trainable for larger-scale QCBMs [43]. In Ref. [12] a more efficient cost function was introduced for gradient-based training of QCBMs. The idea was to compare the distance of the samples drawn from the target and the model distribution in a kernel feature space. This loss function is called the squared maximum mean discrepancy (MMD):

$$\begin{aligned} \mathcal{L}_{\text{MMD}}(P_{\theta}, P^*) &= \left\| \sum_x P_{\theta}(x) \phi(x) - \sum_x P^*(x) \phi(x) \right\|^2 \\ &= \mathbb{E}_{x \sim P_{\theta}, y \sim P_{\theta}} [K(x, y)] + \mathbb{E}_{x \sim P^*, y \sim P^*} [K(x, y)] \\ &\quad - 2 \mathbb{E}_{x \sim P_{\theta}, y \sim P^*} [K(x, y)], \end{aligned} \quad (7)$$

where the ϕ function maps x into a higher dimensional space and by definition $K(x, y) = \phi(x)^T \phi(y)$ is the kernel function, for which they used a Gaussian kernel

$$K_{x,y} = \exp \left(-\frac{1}{2\sigma^2} |x - y|^2 \right). \quad (8)$$

Having a family of parametrized circuits and a cost function to characterize the distance between the circuit output and the target distribution, the final building block is the optimizer, that adjusts the circuit parameters given the cost function. Both gradient-based and gradient-free optimizers have been used to train QCBMs [12, 44]. In our numerical experiments, we only consider gradient-based optimization methods, but since our approach concentrates on Ansatz-design, it is compatible with other optimizers as well.

2. Existing quantum circuit adaptations of PGMs

Liu and Wang [12] made the first explicit connection between the paradigmatic QCBM model and PGMs. They propose a framework, in which they first construct the Chow-Liu tree of a dataset [45] based on the mutual information between all pairs of bits for training samples. Having this tree graph, they propose a QCBM Ansatz, in which, the connectivity pattern of the *CNOT* gates respects the graph structure. The Chow-Liu tree offers an effective approach for creating a second-order product approximation of a joint probability distribution. The corresponding graph represents a BN, that can also be regarded as a pairwise MN, but being a second-order approximation, it fails to detect higher-order correlations. Another explicit connection between BNs and QCBMs was formulated in Ref. [46], where the authors proposed a framework, that utilizes QCBMs for variational inference in PGMs.

Besides the variational framework of general-purpose QCBMs, there have been several attempts to exactly implement PGMs on a quantum computer. BNs have an equivalent formulation in the computational basis measurements of a class of quantum circuits known as Bayesian quantum circuits (BQCs) [34]. These are defined such that the probability distribution they sample from, by measuring the given qubits in the computational basis, corresponds to the distribution defined by the corresponding BN. BQCs are implemented with uniformly controlled gates, that can be decomposed into one-qubit rotations and *CNOT* gates [35, 47]. By definition, these circuits obey certain rules in accordance with the directed, acyclic nature of the underlying graph.

In Ref. [36] the authors introduced a minimal extension to BQCs and presented unconditional proof of separation in the expressive power of BNs and the corresponding basis-enhanced BQCs (BBQCs). They showed that by letting the final measurement be in any local basis, this separation appears, that can be associated with quantum nonlocality and contextuality. They also pointed out, that both BQCs and their basis-enhanced versions can be efficiently simulated with classical tensor network methods, when the graphs are sparse enough.

The literature on the quantum circuit implementation of Markov networks is more scarce. In Ref. [48] the authors identified a novel embedding technique of MNs into unitary operators that relies on their log-linear representation. They construct a Hamiltonian composed of Pauli-Z terms and give a quantum algorithm, that implements the exponential of this Hamiltonian, meaning, that measuring the output qubits of the corresponding quantum circuit is equivalent to sampling the corresponding MN. The circuit, that implements this exponentiation, uses a special point-wise polynomial approximation and real part extraction, that might fail. For this reason, they have to measure ancillary qubits in order to determine whether this extraction was successful and potentially start everything over. Consequently, the success

probability decreases exponentially with the number of maximal cliques. This can of course be amplified with quantum singular value transformation [49], but that further increases the required resources. Since Boltzmann machines form a subclass of pairwise MNs, their quantum circuit implementations can also be regarded as an adaptation of PGMs [17]. However, these models are quite restricted compared to general MNs, since they only consider pairwise correlations, usually in a bipartite manner.

III. QUANTUM CIRCUIT MARKOV RANDOM FIELDS

In this section, we present our results, starting with the definition of our QML model, proposed for generative learning in MNs. We then introduce our novel benchmark proposal and compare our model to both problem-agnostic QCIBMs and BBQCs through a series of numerical experiments. As a preliminary analysis of trainability, we investigate the scaling of the cost function variance for different types of graphs. Finally, we present our argument for a potential quantum advantage of our MN-based model class.

A. From Graphical Representation to Variational Ansatz

We propose a QCBM Ansatz for distribution learning in MNs, as described in Prob. 1. We start by constructing a parametrized many-body Ising Hamiltonian, that is inspired by the log-linear model of MNs, and consequently depends on the clique structure of the MN \mathcal{H} . This Hamiltonian takes the form

$$H'(\beta) = \sum_{C \in \mathcal{C}_H} \bigotimes_{v \in C} \beta_{C,v} (I + Z_v),$$

where Z_v is the Pauli-Z operator acting on qubit v , \mathcal{C}_H refers to the set of cliques and β is the set of parameters. Please note, that the β parameters are only used to enable a compact representation, but ultimately do not reflect the number of free parameters in the final model. Usually some of the MN cliques overlap in non-zero subsets, thus there will be reoccurring terms. Since all terms commute, we can reparametrize the Hamiltonian such that each term only appears once with a distinct coefficient (and identities are excluded): $H'(\beta) \rightarrow H(\alpha)$. Also note, that in this new parametrization, each element of α is independent, in the most general case, and $|\alpha| \geq |\beta|$.

Having formulated this parametrized Hamiltonian, that encodes the structure of the problem, we consider the unitary it generates as

$$U_Z(\alpha) = e^{-iH(\alpha)}, \quad (9)$$

and implement a model similar to QCIBMs, defined in Sec. II B 1 and Fig. 3. We call these problem-informed

QCBM models quantum circuit Markov random fields (QCMRFs). For a more detailed model construction process, please refer to Appendix A, where we rely on the representation of probability distributions as diagonal matrices and use the Pauli expansion of the projectors. Furthermore, we also show that the output probability distribution of the QCMRF model can be factorized according to the same MN, that was used in its construction.

As an example, the MN shown in Fig. 2b defines a 3-local Hamiltonian of the following form: $H(\alpha) = \alpha_1 Z_A Z_B Z_C + \alpha_2 Z_A Z_B + \alpha_3 Z_B Z_C + \alpha_4 Z_A Z_C + \alpha_5 Z_C Z_D + \alpha_6 Z_A + \alpha_7 Z_B + \alpha_8 Z_C + \alpha_9 Z_D$.

Alternatively, one can also limit the locality of the Hamiltonian to get shallower circuits, that in turn can be worse at capturing higher-order correlations. This is ultimately equivalent to considering smaller cliques instead of the maximal clique factorization. The circuit implementation details are discussed in Appendix B 1.

B. Benchmark Proposal

Benchmarking generative QML models often relies on generic probability distributions, such as the bars and stripes dataset, or some Hamming weight specific target distribution [11, 43, 50]. Here, we describe our proposal for constructing target distributions for these models, where the complexity is tunable in several ways. This construction relies on MNs, where the graph structure can be defined by the user. In general, the “difficulty” of the learning problem is proportional to the clique sizes of the MN. The most general case is a complete graph with a single maximal clique, that corresponds to explicitly encoding the probability to each global state.

Given an undirected graph \mathcal{G} , a set of cliques \mathcal{C}_H , and a classical (pseudo)random number generator, we construct a target MN \mathcal{H} , as in Def. 2, through the following steps:

1. To each clique $C \in \mathcal{C}_H$, we assign a factor as a set of $2^{|C|}$ numbers obtained by querying the classical generator $2^{|C|}$ times.
2. Next, we calculate the unnormalized measures of each global assignment by multiplying the corresponding element of each factor table.
3. To get the probability of each assignment, we then normalize the measures by the partition function.
4. Finally, we sample this joint probability distribution classically several times to construct the training dataset \mathcal{D} .

As the size of the graph increases, this procedure becomes highly inefficient, because of the exponential size of the space. In these cases, instead of calculating the target probabilities exactly, steps 2 – 4. can be replaced by the use of approximate sampling techniques to sample

\mathcal{H} directly [31], e.g., by using Markov chain Monte Carlo methods.

Similar steps can be taken for BNs as well, but there one chooses $2^{|Pa_{X_i}^G|}$ random probabilities for each random variable X_i .

The main complexity of the target problem comes from the graph topology and the size of the cliques. This means, that given a graph structure and its maximal clique factorization, we can increase the complexity of the corresponding target distribution by introducing additional edges and considering the maximal cliques of the new graph. The second complexity factor comes from the classical generator, that assigns factor values to the cliques. Throughout our numerical investigations, we sample these values uniformly at random in an IID fashion from a positive range of real numbers. Alternatively, one can consider sampling the factor values from a more complex distribution, as long as classical sampling can be performed efficiently.

C. Numerical Experiments

Here we present two types of numerical experiments: the first kind aims to show, that our QCMRF model performs better than the problem-agnostic QCIBM on structured MNs; in the second set, we compare its performance to BBQCs. In the latter case, we consider loop graphs, that first need to be triangulated in order to implement the corresponding BBQC models.

In all experiments, trainings are carried out with two different cost functions: the KL divergence as in (6) and the MMD loss as in (7), where the kernel function is calculated as the average of 3 different Gaussian kernels with $\sigma \in \{0.25, 10, 10^3\}$. The KL divergence has access to the exact target probability distribution, while the MMD loss can only access a finite training set.

The quantum circuit simulations are carried out with the PennyLane software package [51], and optimized with Adam [52], with learning rate 0.1. We train all models for 500 epochs.

While we use only a finite number of shots for training, the TV distance between the model and target distributions is calculated analytically in each step. We run multiple experiments with different random factor values and analyse the average performance of all models with both cost functions as measured in the exact TV distance. For better visualization, we also average over a window of 20 training epochs.

1. Benchmarks against QCIBMs

To demonstrate the superiority of our model compared to the problem-agnostic QCIBM with all-to-all connectivity, first we present simulation results based on

MNs with grid-like topology, always considering the maximal clique factorization. The number of training samples for the MMD loss along with the number of quantum circuit evaluations was set to 10^4 . We consider 5 sets of uniformly random factor values and take the average performance over these.

All parameters of both models are initialized to 0, as in this setting, the model starts the training in the equal superposition of all basis states. This strategy proved to be better than random initialization.

The results are shown in the top row of Fig. 4. We start with a 3×3 grid, which defines a pairwise MN, meaning, that the corresponding QCMRF model incorporates only 2-local interactions. Here, both models have similar performance, while our QCMRF model reduces the number of trainable parameters from 72 to 48.

We continue by introducing additional edges to the grid. All the maximal cliques of the second graph have size 3, leading to a 3-local Hamiltonian, that can capture higher-order correlations. Here we can already see some separation in the performance, while still having less parameters (60) than the QCIBM. In the last case, the cliques are of size 4, which increases the number of trainable parameters in the QCMRF circuit to 76. In this case, our model significantly outperforms the 2-local QCIBM.

This series of experiments show, that as we increase the connectivity of the graph and the sizes of its maximal cliques, the distribution becomes harder to learn, as it is reflected in the performance of the problem-agnostic QCIBM. However, the performance of our problem-specific QCMRF model is either unaffected by this change, or it performs even better, as its complexity also increases with the underlying MN. This also proves, that using higher-order Hamiltonians can actually help in capturing higher-order correlations between the random variables of the MN.

Next, we focus on random graphs, that are globally less structured, thus being closer to naturally occurring topologies. Here we explore the role of communities. By communities, we refer to dense subgraphs, that are sparsely connected between each-other. The results are shown in the bottom row of Fig. 4, where the training is done similarly to the previous experiments. Here our QCMRF models reach better performance than the problem-agnostic QCIBMs, while significantly reducing the number of trainable parameters, since they exploit the sparsity of the graph. For these 10-node graphs, the corresponding QCIBM model has 85 parameters, while the QCMRF circuits only have 60, 58 and 66 respectively. Furthermore, in the third graph, where the communities are connected by a node with large centrality measures, the QCMRF model significantly outperforms the problem-agnostic case. These experiments further prove the usefulness and viability of our Ansatz design approach.

We also showcase the scaling of the performance separation with the number of qubits for a triangle chain

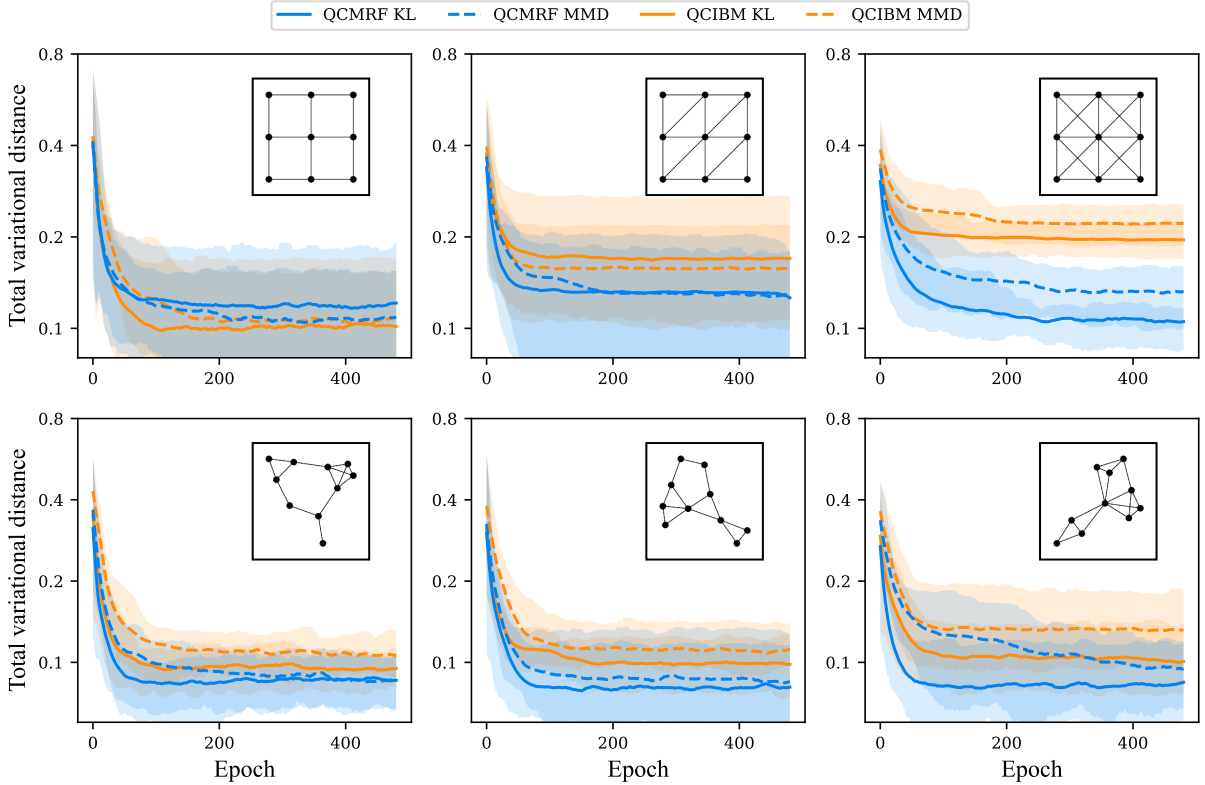


FIG. 4. **QCMRF benchmark results against the problem-agnostic QCIBM model using KL divergence and Maximum Mean Discrepancy (MMD) loss functions.** In the case of grid topologies (top row), as the complexity of the problem increases by using larger maximal cliques, the performance of the QCIBM model decreases, while QCMRFs are either unaffected by this or even improve, as they also increase their complexity. The structured random graphs (bottom row) have densely connected communities, but the connectivity of these subgraphs is sparse. In this case, the QCMRF models still show good performance, significantly reducing the number of trainable parameters, but also improving the performance when the communities are connected by a node with large centrality measures (last graph).

graph. These results based on exact simulation (infinite shot limit) are shown in Appendix D, where we also present a minimal numerical comparison to classical methods.

2. Benchmarks against BBQCs

Next, we validate our model with BBQCs on non-chordal MNs. In these cases, the undirected graph first has to be triangulated and turned into a directed acyclic graph. Knowing the structure of this BN, one can implement the corresponding BBQC, that is able to capture the target distribution exactly. However, this process is very costly: the triangulation of the graph itself is a hard problem, and it can introduce a large number of edges, that leads to the introduction of additional variables. Consequently, the corresponding BBQC can have many more trainable parameters and the circuit depth can be significantly larger.

For this comparison, we considered loop graphs, that are easy to triangulate. Since with 0 parameter

initialization, the starting probability distribution is different for QCMRF and BBQC circuits, here we started with random values to have a more fair comparison. The number of shots was set to 10^3 for all experiments, along with the size of the training set for the MMD-based optimizations. We ran all experiments with 10 sets of uniformly random factor values and visualized the average performance in Fig. 5.

All these loop-graphs can be used to implement QCMRF circuits, while to define the corresponding BBQC, the triangulation introduces $n-3$ new edges. Due to this fact, the number of trainable parameters along with the depth of the circuit is significantly increased. In all cases, our MN-based model reaches similar performance to BBQCs, while having much lower cost of implementation, which further highlights the usefulness of our model class. For a deeper comparison between the implementation costs of these models, we refer the reader to Appendix C.

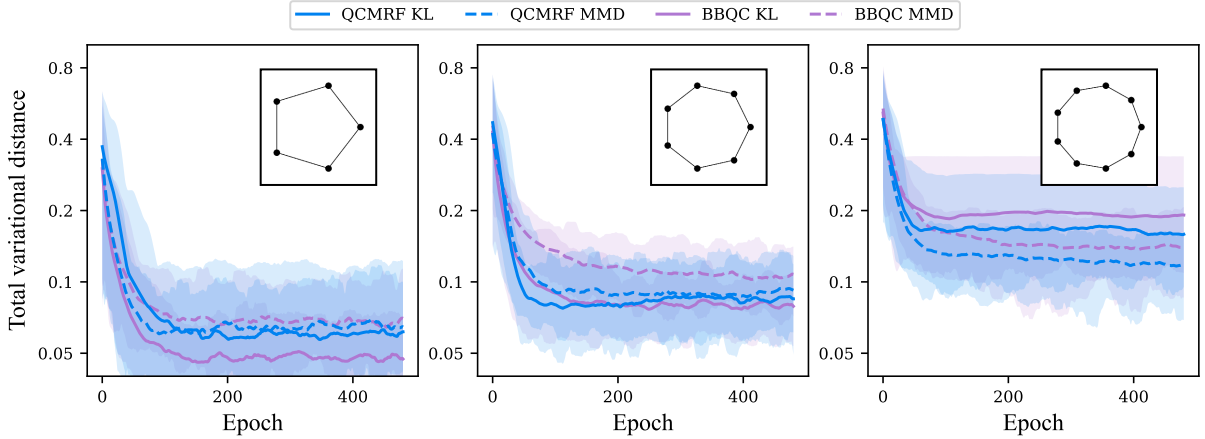


FIG. 5. **Validating results against BBQC models on loop graphs.** The QCMRF models reach comparable performance to the BBQCs, while requiring less parameters and much shallower circuits. This difference is associated with the fact, that these graphs have to be triangulated before implementing the corresponding BBQCs.

D. Trainability

While MNs are capable of representing any probability distribution, we expect that not all types of networks lead to efficiently trainable QML models. For this reason, we conduct a preliminary analysis of the trainability properties of QCMRFs. In particular, we study numerically the scaling of the MMD cost function variance with the number of qubits (or nodes). Having fixed the graph type, for each number of nodes, we define 10 sets of uniformly random factor values and in each case, we evaluate the variance using 10^4 sets of random circuit parameters. The cost value is calculated with a training set of 10^4 samples and 10^4 quantum circuit evaluations.

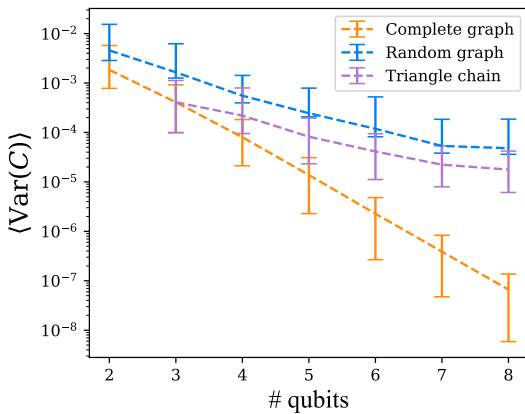


FIG. 6. **Scaling of the cost variance for 3 types of MN graphs.** Dashed lines connect the average variance over 10 sets of random factor values, while the error bars show the minimum and the maximum for a given graph-type and number of qubits.

A complete graph having maximal clique factorization corresponds to no structure, since the probability

distribution has $2^n - 1$ degrees of freedom. As shown in Fig. 6, according to our numerics, the cost function variance vanishes exponentially in the number of qubits in this case, which also indicates the presence of deterministic barren plateaus [53]. To study sparser (but still dense) graphs, we concentrate first on Erdős-Rényi graphs with $p = 0.5$ edge probability, since in this case, the expected size of the largest clique is $\mathcal{O}(\log n)$ with high probability. Our simulations clearly show, that the variance exhibits much better scaling in this case, than the conclusively exponential decay before. This is also true for triangle chain graphs, where we have $n - 2$ cliques of size 3 in total. While cost concentration and gradient concentration go hand in hand in variational quantum algorithms, polynomial scaling in the cost variance can be induced by a few parameters with good behaviour [53, 54]. Consequently, such a polynomial scaling does not show the empirical absence of barren plateaus, but it is a good first indicator of better trainability.

These investigations lead us to the definition of a subclass of MNs, that restrict the class of problems, that our problem-informed framework can be most useful for.

Definition 3 (Efficient MN representation). *A probability distribution P_Φ over n binary random variables is said to have an efficient MN representation, if P_Φ factorizes according to a Markov network \mathcal{H} with*

$$\sum_{C \in \mathcal{C}_\mathcal{H}} 2^{|C|} \in \text{poly}(n),$$

where $\mathcal{C}_\mathcal{H}$ is the set of cliques of \mathcal{H} .

It follows naturally from our definitions, that QCMRF circuits, corresponding to efficient MN representations, have depth $\text{poly}(n)$.

E. Potential for Quantum Advantage

Quantum advantage, in the context of generative learning, can have various flavours: it can show improvement in the precision (with respect to a distance metric); it can refer to faster convergence; or even an improvement in the number of training samples needed. In order to formulate all these cases in a single definition, we first need to define what we mean by a class of distributions being efficiently learnable:

Definition 4 *((d, ε, k, C)-learnable).* *For a metric d , $\varepsilon > 0$, $k > 0$ and complexity class C , a class of distributions P^n is called $((d, \varepsilon, k, C)$ -learnable, if there exists an algorithm $\mathcal{A} \in C$, that given $0 < \delta < 1$ as input and having access to a dataset \mathcal{D} of size k sampled from any $P \in P^n$, outputs with probability at least $1 - \delta$ a representation of a distribution $P_{\mathcal{M}}$ satisfying $d(P, P_{\mathcal{M}}) \leq \varepsilon$. \mathcal{A} should run in time $\text{poly}(1/\varepsilon, 1/\delta, n)$.*

With this, we extended the definition from [13] with the sample complexity, and now formulate quantum learning advantage:

Definition 5 *(Quantum Learning Advantage).* *An algorithm $\mathcal{A} \in BQP$ is said to have quantum learning advantage, if there exists a class of distributions P^n for which there exists d, ε, k such that P^n is $((d, \varepsilon, k, BQP)$ -learnable, but not $((d, \varepsilon, k, BPP)$ -learnable, where this concept of learnability is defined in Def. 4.*

Besides learning advantage, generative QML models also have the potential to exceed classical methods for sampling the learned distribution:

Definition 6 *(Quantum Advantage in Sampling).* *Given a probability distributions $P_{\mathcal{M}1}$ satisfying $d(P, P_{\mathcal{M}1}) \leq \varepsilon$ (for some d metric and $\varepsilon > 0$), a quantum algorithm $\mathcal{A}_1 \in BQP$ is said to have quantum advantage in sampling from the distribution P , if \mathcal{A}_1 can efficiently sample $P_{\mathcal{M}1}$ and no classical algorithm $\mathcal{A}_2 \in BPP$ can sample $P_{\mathcal{M}2}$ efficiently, where $d(P, P_{\mathcal{M}2}) \leq \varepsilon$.*

In the following, we concentrate on this second definition and argue, that since our QCMRF model class contains the class of QAOA and IQP circuits, it can also produce distributions that are thought to be classically hard. For this, we assume, that the joint distribution of a target MN is learnable by both an arbitrary classical model and a QCMRF model to a given precision ε and analyse the complexity of sampling the trained models. Previous works [13, 55] presented similar arguments, relying on the results of Refs. [7, 56]. We start by sketching current results regarding the hardness of sampling QAOA circuits, then based on this, we present our conjecture about the possible quantum advantage in sampling for our model.

The Quantum Approximate Optimization Algorithm (QAOA) was proposed in Ref. [37] for approximately solving combinatorial optimization problems on

a quantum computer. In [7], the authors proved, that efficient classical sampling of the output distribution of the 1-level QAOA circuit implies the collapse of the polynomial hierarchy to the third level. While the argument was constructed with a 2-local QAOA circuit, the proof stands for higher-order Z interactions as well, all these being diagonal operators. On the other hand, this was shown for multiplicative error only, meaning, that if the target distribution (being the one defined by the QAOA circuit) P_{QAOA} and the classical model distribution $P_{\mathcal{M}}$ satisfy the bound

$$|P_{\mathcal{M}}(x) - P_{QAOA}(x)| \leq \varepsilon P_{QAOA}(x), \forall x, \quad (10)$$

then the polynomial hierarchy collapses to its third level. In our framework, however, we mostly concentrated on distance as measured in TV, which is equivalent to additive error. Multiplicative error is a stronger constraint, thus simulating up to a bounded additive error is a harder task. These results using multiplicative error were extended in Ref. [57] from worst case to average case hardness for 1-level QAOA circuits. Finally, in Ref. [38], the author proved average case hardness with additive error, which, up to our knowledge, is the strongest result in connection with the weak simulation of 1-level QAOA circuits. Since the class of probability distributions defined by the output of QCMRF circuits contains the 1-level QAOA circuits, this larger class can also be hard to weakly simulate, i.e., to sample the output probability distribution efficiently classically. This also means, that - provided that we can train a QCMRF model to sufficient precision - we can use the trained model to efficiently sample the distribution of the underlying MN. These facts together with our numerical findings lead to the following conjecture.

Informal Conjecture. *The class of QCMRF circuits, that can learn probability distributions efficiently represented by MNs, also contains classically hard cases, yielding a quantum advantage in sampling.*

IV. CONCLUSION & OUTLOOK

In this work, we highlighted the potential of probabilistic graphical models for generative QML. We introduced a framework for constructing quantum circuit Born machine Ansätze, that respect the structure of the Markov network describing the underlying problem. A novel problem construction process was presented for benchmarking generative QML models, where the complexity of the learning task can be tuned in various ways. This benchmarking framework is capable of constructing explicit distribution learning problems and more realistic tasks based on limited samples.

Our numerical experiments demonstrated that our model, called quantum circuit Markov random field, is capable of capturing higher-order correlations between the binary random variables of the corresponding MN. This can significantly improve the performance

in the case of higher-order target models, while potentially reduce the number of trainable parameters on sparse graphs, compared to problem-agnostic approaches. We further validated our model with basis-enhanced Bayesian quantum circuits on non-chordal MNs, since these BN-based models are able to express the target distribution exactly. The QCMRF models reached the performance of BBQCs on small loop-graphs with fewer parameters and significantly shallower circuits. All these experiments were conducted using the KL divergence and MMD loss functions, to demonstrate both exact distribution learning tasks and more practical generative learning based on limited training samples.

A preliminary numerical analysis of trainability was presented, that introduced an important constraint on the sparsity of the potential MNs of interest. We formulated two definitions of quantum advantage, relevant in the context of generative models, where the first concentrated on a learning advantage (Def. 5), and the second focused on efficiently sampling from the learned distribution (Def. 6). We presented an argument in the second setting, highlighting the potential of our model to offer improvements over classical methods, since it contains the class of QAOA circuits, that are known to be hard to sample classically. We also believe that this connection between classical MNs and QAOA-type circuits opens up an interesting direction for further investigations.

While we concentrated on learning a target distribution to high accuracy, this alone is not enough to characterize the performance of generative models. Another important factor is the model's ability to generalize, rather than memorize the training data [58]. In the context of PGMs, this can be investigated with a training dataset of limited size, assessing the trained model's ability to generate valid but unseen samples. We also remark, that while our QCMRF model shows significant improvement compared to problem-agnostic QCIBMs on several small examples, BBQCs show better performance on chordal graphs, where both PGM-based models have the same number of trainable parameters. This means, that for chordal graphs, BN-based models are better at capturing the target distribution, although requiring much deeper circuits. Finally, what can be seen as a major setback of our framework is that it assumes knowledge of the graph structure along with its cliques. While this seems like a major obstacle, this knowledge is readily available in various use cases. Furthermore, this generative QML approach can be used together or as a subroutine of classical structure learning algorithms [59].

Possible extensions of our QCMRF model could include replacing the final set of general one-qubit unitaries $U_f(\Gamma, \Delta, \Sigma)$ with one-parameter rotations (e.g., R_X rotations), as well as using multiple layers to have higher resemblance to QAOA circuits and to reach the over-parametrized regime. Finally, we also remark that, while our model design framework was constructed in the context of QCBMs, this idea can also help in designing other

generative QML models, e.g., QGANs.

ACKNOWLEDGEMENTS

The authors would like to thank the support of the Hungarian National Research, Development and Innovation Office (NKFIH) through the KDP-2021 and KDP-2023 funding scheme, the Quantum Information National Laboratory of Hungary and the grants TKP-2021-NVA-04 and FK 135220. Z.Z. was partially supported by the Horizon Europe programme HORIZON-CL4-2022-QUANTUM-01-SGA via the project 101113946 OpenSuperQPlus100 and the QuantERA II project HQCC-101017733. The authors also acknowledge the computational resources provided by the Wigner Scientific Computational Laboratory (WSCLAB).

Appendix A: Ansatz design

Here we give a more detailed description of our QCMRF Ansatz design process. Let us consider a single clique C , with factor ϕ_C , and embed the corresponding marginal probability distribution in the diagonal of a $2^{|C|} \times 2^{|C|}$ matrix as

$$\begin{aligned} H_C &= \text{diag}(P_{\phi_C}) \\ &= \frac{1}{Z_{\phi_C}} \sum_{x \in 2^{|C|}} \phi_C(x) |x\rangle\langle x| \\ &= \frac{1}{Z_{\phi_C}} \sum_{x \in 2^{|C|}} \phi_C(x) \bigotimes_i \frac{1}{2} (\mathbb{1}_i + (-1)^{x_i} Z_i). \end{aligned} \quad (\text{A1})$$

Here Z_{ϕ_C} denotes the normalizing constant of the marginal distribution, $|C|$ denotes the size of clique C , and in the last line, we used the Pauli expansion of the projectors.

We can reparametrize this linear combination of Pauli strings as

$$\begin{aligned} H_C(\boldsymbol{\alpha}) &= \alpha_0 \bigotimes_i \mathbb{1}_i + \alpha_1 Z_0 + \alpha_2 Z_1 + \dots \\ &\quad + \alpha_{2^{|C|}-1} \bigotimes_i Z_i. \end{aligned} \quad (\text{A2})$$

After discarding the identity term, we consider the unitary $U_C(\boldsymbol{\alpha}) = \exp(-iH_C(\boldsymbol{\alpha}))$. At this point, it is easy to see, that if this operator acts on the initial state as $U_C(\boldsymbol{\alpha}) |+\rangle^{\otimes n}$, then the marginal probability distribution is encoded into the phases of each computational basis state. We can also see, that there are $2^{|C|} - 1$ parameters, which is exactly how many degrees of freedom a probability distribution over $|C|$ binary random variables has.

Going back to the full probability distribution P_{Φ} , that factorises according to a MN as in Def. 2, we can

embed this into the diagonal of a $2^n \times 2^n$ matrix of the

form

$$\begin{aligned}
 H = \text{diag}(P_\Phi) &= \frac{1}{Z_\Phi} \prod_{C \in \mathcal{C}} \left[\sum_{x < 2^{|C|}} \phi_C(x) \bigotimes_{i \in C} \frac{1}{2} (\mathbb{1}_i + (-1)^{x_{C(i)}} Z_i) \bigotimes_{i \notin C} \mathbb{1}_i \right] \\
 &= \frac{1}{Z_\Phi} \sum_{x < 2^n} \left[\prod_{C \in \mathcal{C}} \phi_C(x_C) \bigotimes_{i \in C} \frac{1}{2} (\mathbb{1}_i + (-1)^{x_i} Z_i) \bigotimes_{i \notin C} \mathbb{1}_i \right].
 \end{aligned} \tag{A3}$$

The first two lines show equivalent definitions, where $C(i)$ denotes the index of node i in clique C and x_C denotes the bits in the binary form of x , that correspond to clique C .

According to the previous argument, after reparametrizing this Hamiltonian as before, the unitary $U_Z(\alpha) = \exp(-iH(\alpha))$ is expressive enough to encode the marginal probability distributions over each clique. However, since the factors are not normalized in general, the joint distribution is not necessarily the same as the factor product of the marginal ones. For this reason, instead of extracting the phases of the state $U|+\rangle^{\otimes n}$, we perform a measurement on each qubit in any local basis, i.e., we apply general one-qubit gates before measurement, where these gates have independent trainable parameters. We expect, that this expressivity enhancement provides enough flexibility to compensate for the mismatch coming from the different scale of the marginal distributions.

We can also take the opposite route and analyse the output probability distribution of this quantum circuit model. We want to analyze the structure of the MN, that factorizes this probability distribution. First, we can write the marginal probability of each random variable in the output distribution as

$$P(X_i) = -\frac{\langle Z_i \rangle - 1}{2}, \tag{A4}$$

where $\langle Z_i \rangle$ denotes the expectation value of the Pauli-Z operator on qubit i . Thus, it suffices to examine the backward light-cone of observable Z_i for all i . Due to the structure of the QCMRF model, the entangling gates in the U_Z operator can be ordered in such a way, that the light-cone of the local observable Z_i only contains the qubits, it is directly connected to, through multi-qubit gates. This means, that the probability in Eq.(A4) can be written as a product of probabilities and conditional probabilities involving only the neighbours of node i . This is equivalent to the Markov property, stating that random variable X_i is conditionally independent of all other variables given its neighbours.

Since in U_Z , all operator terms commute, each ordering of the gates (generated by the tensor product of Pauli-Z operators) produces the same quantum state leading to the same output probability distribution.

Therefore, the Markov property applies to all output random variables simultaneously. Due to the Hammersley-Clifford theorem for strictly-positive probability distributions [60], the presence of this Markov property also means, that the joint probability distribution factorizes according to the corresponding MN. Consequently, the output probability distribution of QCMRF circuits factorizes according to the same MN structure, assuming positive probabilities.

Appendix B: Implementation details

In this section, we describe the implementation details of the PGM-based quantum models, including possible decompositions of multi-qubit operators into single-qubit and $CNOT$ gates.

1. Quantum Circuit Markov Random Fields

Markov networks define higher-order Ising Hamiltonians as described in III A, which generate QCMRF circuits composed of *MultiRZ* gates. For the MN in Fig. 2b, the corresponding parametrized circuit is shown in Fig. 7a. A k -local *MultiRZ* gate can be implemented in linear depth with $2k$ $CNOT$ gates and a single-qubit R_Z rotation. An example for this decomposition is shown in Fig. 7b. There are several other alternative strategies for implementing these circuits, as explained in the context of QAOA in Refs. [61, 62]. For example, one could implement the circuit corresponding to a clique with m random variables with significantly fewer $CNOT$ gates using an ancillary qubit, as shown in Fig. 7c. This approach reduces the number of gates and the depth, while adding an ancillary qubit for each clique of size > 2 .

The implementation of the QCIBM circuit can be done similarly, only using 2-local *MultiRZ* gates, that do not need any ancillary qubits.

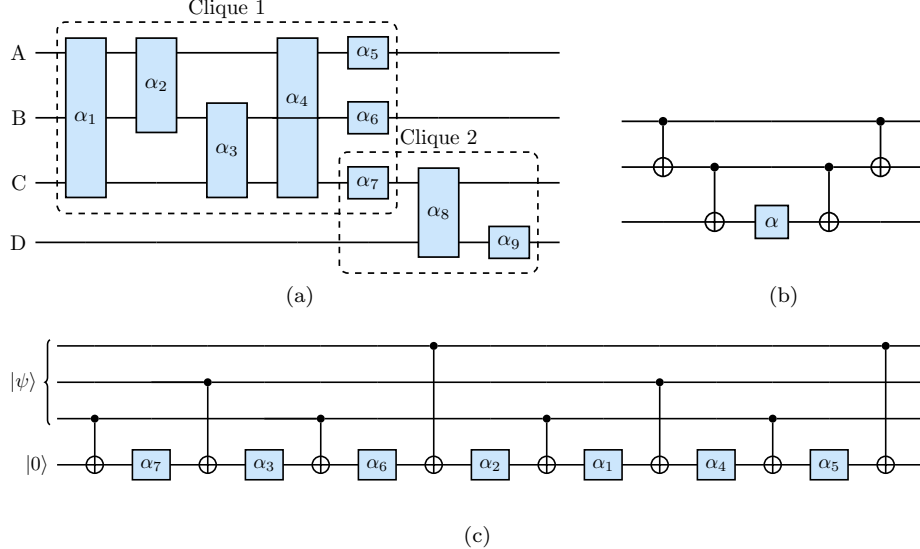


FIG. 7. **Decomposition of U_Z operators generated by many-body Ising Hamiltonians.** (a) Complete $U_Z(\alpha)$ operator corresponding to MN in Fig. 2b. (b) Decomposition of $\exp\{-i\alpha ZZZ\}$, a 3-body *MultiRZ* gate parametrized by α . (c) Implementation of all terms of a clique of size 3 with an additional ancillary qubit. In all the figures, parametrized gates represent k -local *MultiRZ* operators.

2. Bayesian Quantum Circuits

Here we start by describing the general idea of BQCs introduced in Ref. [34]. This model associates a qubit to each binary random variable of the BN and then applies unitary operations in the following manner. First parametrized single-qubit R_Y rotation gates are applied to qubits for which the corresponding nodes have no parents. Then uniformly controlled R_Y operations are performed on each qubit, where the control qubits correspond to the parents of the given node. Note, that since a node can have multiple parents, this can lead to gates with a large number of controls. The order of application of these unitaries has to follow two rules: every qubit can only be targeted once and after a qubit was used as a control, it cannot be targeted any more. These rules ensure the compliance with the directed acyclic nature of the graph. The basis-enhancement introduced in Ref. [36] further applies parametrized general $U_f(\Gamma, \Delta, \Sigma)$ gates to all qubits. The BBQC corresponding to the BN presented in 2a is shown in Fig. 8a.

While uniformly controlled gates provide an easily interpretable mapping from the BN graph to a parametrized quantum circuit, they cannot be implemented directly. The number of parameters for such a gate is 2^{n_c} , where n_c is the number of control qubits. In Ref. [35] and [47], the authors gave several strategies to decompose these operators. For the purpose of this work, it is easiest to think of these as the decomposition in terms of (multi-controlled) R_Y rotations and X gates. This decomposition of a uniformly controlled R_Y rotation with 2 controls is shown in Fig. 8b. The multi-controlled gates can be further decomposed into single qubit rota-

tion and $CNOT$ gates with additional ancillary qubits as described in Ref. [35] or by adapting the ancilla-free strategy of [63].

Appendix C: Resource estimation

Here we review the general cost of implementation, considering the number of parameters, qubits and the circuit depth. We compare these metrics for all three models, where possible.

1. Number of parameters

An important factor in QML Ansatz design is the number of trainable parameters. This consideration leads to a delicate balance. On one hand, we want our model to have enough expressivity to capture the target distribution. On the other hand, we want to limit the number of parameters, to provide faster training, minimize noise and potentially escape barren plateaus [20, 21].

In the case of the QCIBM and QCMRF models, the number of parameters depends mostly on the number of terms in the Hamiltonian that generates the time evolution. However, these models cannot be compared directly, since in QCIBMs this number only depends on the number of qubits n and in QCMRF circuits there is an explicit dependence on the graph topology and the clique factorization, but also the overlap of the cliques.

To represent a classical MN as complete factor-tables, one needs $\sum_{C \in \mathcal{C}} 2^{|C|}$ parameters, $|C|$ referring to the size of clique C . Consequently, our Hamiltonian be-

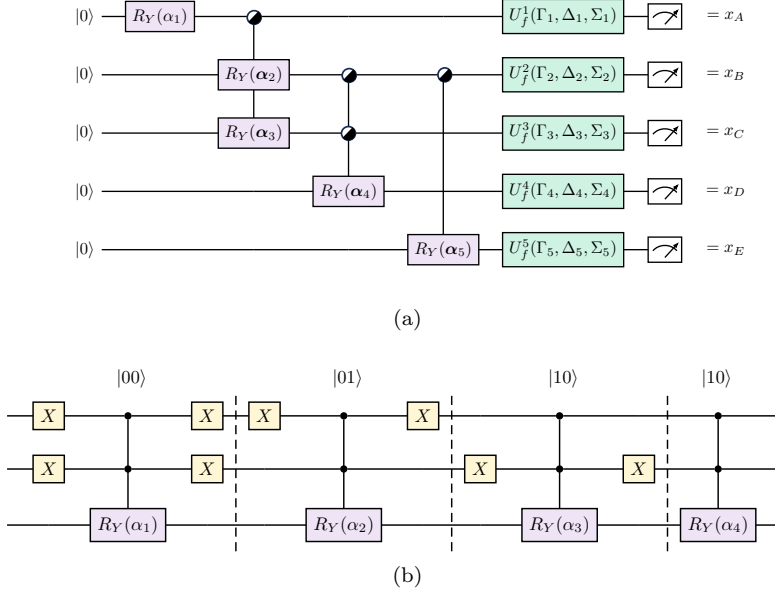


FIG. 8. **Implementation of BBQC circuits.** (a) Complete BBQC circuit corresponding to BN in Fig. 2a (b) Decomposition of a uniformly controlled R_Y rotation gate, parametrized with parameter vector α , having two control qubits. The number of multi-controlled R_Y rotations scales exponentially with the number of controls. Half-empty controls denote uniformly controlled gates.

fore reparametrization has exactly these many parameters. This means, that the parameter count in a QCMRF Ansatz is

$$k_{QCMRF} \leq \sum_{C \in \mathcal{C}} \sum_{k=1}^{|C|} \binom{|C|}{k} + 3n = \sum_{C \in \mathcal{C}} (2^{|C|} - 1) + 3n. \quad (\text{C1})$$

We can see, that this number does not depend on the problem size, i.e. the number of binary random variables n directly, only on the sizes of the cliques l_C . This means, that assuming the clique sizes of a given graph topology is constant, without explicit dependence on the number of nodes, the parameter count is $\mathcal{O}(n)$.

In the case of the problem-agnostic 2-local QCIBM Ansatz, this number is $k_{QCIBM} = n(n-1)/2 + 4n$, which is $\mathcal{O}(n^2)$.

It is worth mentioning, that for pairwise MNs, meaning those defined by only pairwise interactions, lead to two-body terms between the qubits representing connected nodes and one-body Pauli-Z terms on all qubits. These give rise to QCMRF circuits with less or equal number of parameters than the corresponding QCIBM Ansatz, where we have equality only for complete graphs.

A similar analysis can be performed for BBQC circuits as well. Here the number of parameters is exactly

$$k_{BBQC} = \sum_{i=1}^n 2^{|Pa_{X_i}^G|} + 3n, \quad (\text{C2})$$

where $|Pa_{X_i}^G|$ refers to the number of parents of the i -th node.

Since the conversion between BNs and MNs can introduce additional edges, this conversion can also introduce additional parameters. This means, that usually, the number of parameters in BBQCs is larger than in QCMRFs, when the underlying problem is defined by a MN. However, for chordal MNs, having maximal clique factorization, the number of parameters in the two model classes is equal.

2. Number of qubits

Since in all the models we consider, we map n binary random variables to n qubits. This means, that the number of qubits in all these cases is n , but certain gate decompositions require ancillary qubits, increasing this number.

For the QCIBM models, since they only contain one- and two-qubit gates, we need no additional ancillas and the final number of qubits is n . In the case of QCMRF circuits we have at least two options, we can use no ancillas leading to the same number, or we can use n_C ancillas, where n_C refers to the number of cliques, that are larger than 2. In this latter case, we end up with $n + n_C$ qubits. We have even more freedom for BBQC models. We can use the ancilla-free implementation of multi-controlled gates from [63], or we can use $l - 1$ ancillary qubits to implement each multi-qubit gate with l controls, where the ancillas can also be reused. It is also possible to interpolate between the two approaches, n and $n + \sum_{i=1; |Pa_{X_i}^G| \neq 0}^n (|Pa_{X_i}^G| - 1)$. This lead to a trade-off between the number of qubits and circuit depth.

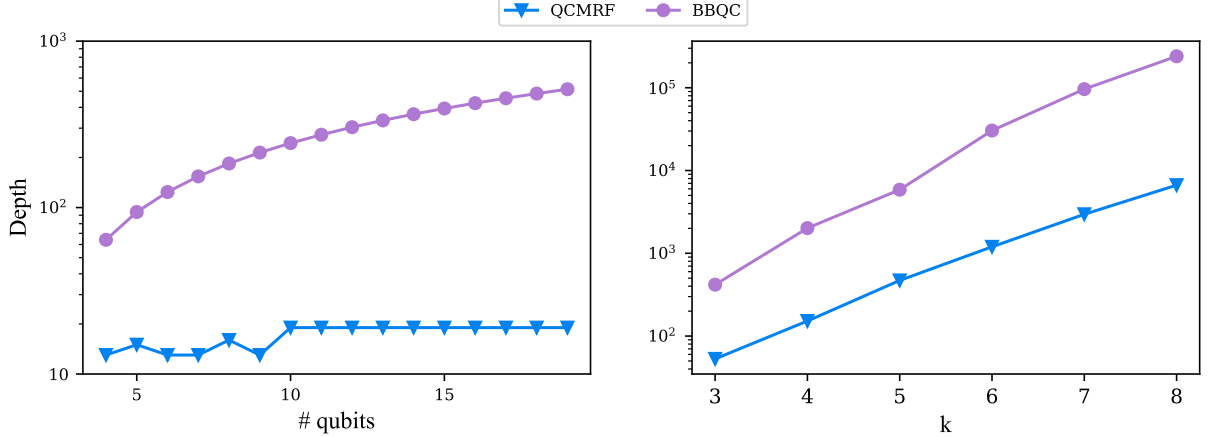


FIG. 9. **Numerical comparison of circuit depth between QCMRF and BBQC models.** The quantum models corresponding to the given graph were transpiled using Qiskit with optimization level 3. Scaling in the number of qubits for loop graphs (left). Scaling in the size of the maximal cliques for k -gram models (right).

3. Circuit depth

Based on the implementation of multi-qubit gates, the depth of the circuit can also vary. In general, the more ancillas we use for decomposing these unitaries, the shallower the final circuit can be. For a fair comparison, here we only consider ancilla-free implementations and analyse the depth accordingly. We also assume full connectivity of qubits and parallel execution of gates that act on disjoint sets of qubits, where possible, and use parametrized one-qubit U_f and $CNOT$ gates as our basis gate set.

QCIBM circuits being problem agnostic, their depth can be estimated knowing only the number of qubits. The initial Hadamard gates along with the single-qubit R_Z rotations and final U_f gates can be implemented in constant depth. Since we assume parallel execution of gates and each two-qubit $\exp(-i\alpha ZZ)$ gate can be implemented in depth 3, the depth of the whole circuit scales $\mathcal{O}(n)$.

For QCMRF circuits, the scaling is more complicated, since it depends on the clique-structure of the MN. Here we give an upper-bound on the depth, considering the Hamiltonian before reparametrization. For each clique C , we have $2^{|C|} - 1$ *MultiRZ* gates, and there are $\binom{|C|}{k}$ k -local gates for each $k \leq |C|$. To minimize the depth, we can implement two gates in parallel in each step, such that the qubits they act on are complements of each other in the clique. In the ancilla-free case, each k -local gate can be implemented in $2k - 1$ depth. This means, that the depth required to implement such a clique is $\mathcal{O}(2^{|C|})$. If we assume $|\mathcal{C}|$ cliques in the graph and the size of the largest maximal clique is l_m , then the depth required is $\mathcal{O}(|\mathcal{C}|2^{l_m})$. However, this is a crude upper bound in the worst case, not taking into account the parallel execution of gates of disjoint cliques. In practice, this scaling can be much better.

The analysis is similar for the BBQC models. Here for each node X_i the number of multi-controlled R_Y gates scales $\mathcal{O}(2^{|Pa_{X_i}^G|})$. Another difference is that we cannot implement these unitaries in parallel, which further increases the depth. By fixing the largest number of parents as n_m^p , the depth scales $\mathcal{O}(n2^{n_m^p})$ in the worst case. It is easy to see, that for BNs and MNs based on chordal graphs, the size of the largest clique is equal to the maximal number of parents.

We compare these two models on the simple, yet illustrative example of a graph composed of a single triangle. This is obviously a chordal graph, and the number of trainable parameters is equal in both circuit. In this case, the depth of the QCMRF circuit is 16. In the corresponding BN, the first node has no parents leading to depth 1. The second node has 1 parent, leading to 2 single-controlled R_Y gates, each implemented in depth 4, thus depth 10 with the X gates. The final node has 2 parents, meaning 4 multi-controlled gates with two controls, each having depth 14, thus depth 60 in total. The final depth of this circuit is 72 with the U_f gates before measurement. This example shows that BBQCs can be much deeper than QCMRF circuits on chordal graphs, while this is not reflected in the number of trainable parameters.

We further demonstrate this difference numerically on two types of graphs. In each case, we compiled the circuits to the given basis gate set using the transpilation method of Qiskit [64] with optimization level 3. First, we explore the scaling in the number of nodes for the loop graphs shown in Fig. 5. Here we can see linear dependence in the case of BBQC and $\mathcal{O}(1)$ for QCMRF, which is expected for this very special type of graph (see Fig. C1 left). While these loops capture an important class, they do not provide a fair comparison, since here the triangulation of the undirected graph introduces a significant number of additional parameters for the corresponding

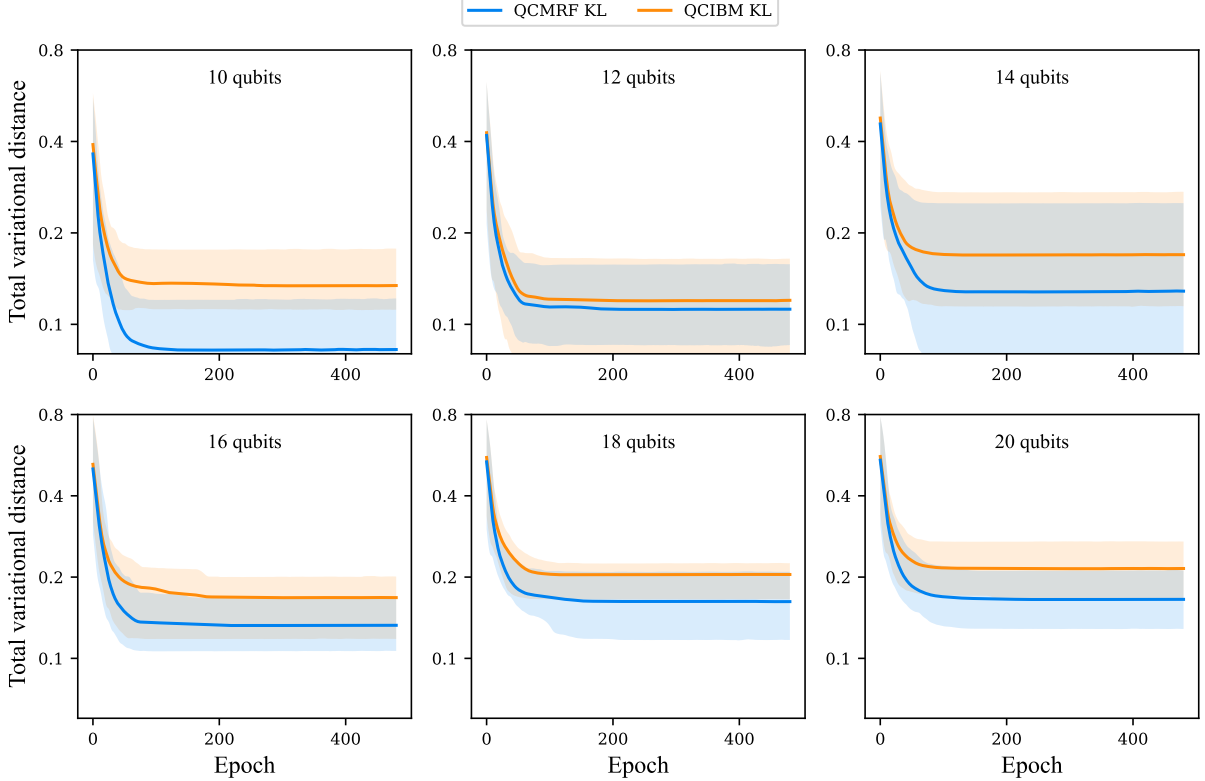


FIG. 10. **QCMRF benchmark results against the problem agnostic QCIBM model using KL divergence and exact quantum circuit simulation.** These training curves show the evolution of the cost function leading to the final TV distance in Fig. 11.

BBQC.

As a next comparison, we concentrate on an important class of BNs, called k -gram models, used in natural language processing applications [65]. In the graph representation of a k -gram model, the nodes form an ordered set, in which the parents of the l -th node are nodes $\{l - k + 1, \dots, l - 1\}$, where they exist. This induces the factorization

$$P(X_1, \dots, X_n) = P(X_1)P(X_2|X_1)P(X_3|X_1, X_2) \dots \cdot P(X_n|X_{n-k+1}, \dots, X_{n-1}). \quad (C3)$$

These models define chordal graphs, where the number of parameters is the same in both quantum models and the maximal number of parents in the BN is the same as the size of the maximal cliques in the corresponding MN. We can observe similar scaling in k for both models, as shown in Fig. C1 (right), but the depth of BBQCs is always at least an order of magnitude higher than that of QCMRF circuits. While this is not significant in a complexity theoretic perspective, it makes a significant difference when implementing on real quantum hardware, especially on near-term devices.

Appendix D: Additional numerical simulations

1. Scaling with exact simulation

We also present experiments based on exact simulation, i.e., exact probabilities corresponding to infinitely many shots. Here we only consider the KL divergence based on the exact model and target probability distributions. While this training is not realistic, as it requires the exact probabilities from both distributions, this way, the simulation can be scaled up to larger problems, than the ones considered in the main text.

For this comparison, we use the triangle chain graph, that is equivalent to the 3-gram model, as in Eq. (C3), each clique being of size 3. In Fig. 10, we present all the training curves with similar hyperparameters as in the simulation in the main text. We show the average of 5 independent problems, having different sets of factor values. The performance scaling with the number of qubits is shown in Fig. 11. Here, we define the final TV distance as the average of the last 100 training epochs in each case. In this figure, markers show the average final TV distance among the 5 problems, and errorbars show the standard deviation around the mean.

The separation in the average performance between the QCMRF and QCIBM models is independent of

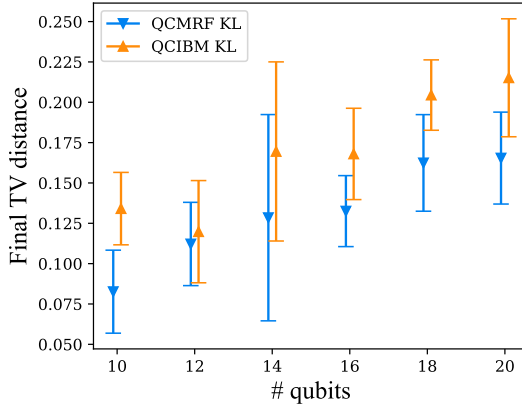


FIG. 11. **Scaling of the final TV distance with the number of qubits using the KL divergence.** Here we use triangle chain graphs, that correspond to 3-gram models. The markers show the average final TV distance of 5 independent problems and errorbars show the standard deviation.

the problem size, while the number of parameters is $\mathcal{O}(n)$ and $\mathcal{O}(n^2)$ respectively. For 20 qubits, this amounts to 135 and 270 parameters.

2. Comparison with classical methods

While we concentrate on comparing QCMRF to other quantum models, here we also provide a preliminary comparison with a classical method. We consider the grid graph topology with 9 nodes, and turn the corresponding MN into a BN. The parameters of the resulting BN are fitted to the training set using maximum likelihood estimation, as implemented in the pgmpy Python package [66]. After fitting, the classical model to the data, we calculate the corresponding probability distribution exactly and compute the TV distance from the target distribution. We repeat this procedure for 100, 500 and 1000 training samples. The corresponding results are shown in Fig. 12. Similarly, the QCMRF models are trained with the same number of training samples, using the MMD loss function. In each case, we run 5 independent problems and plot the results similarly to previous experiments.

While our model shows similar performance with small training sets, its performance is weaker when the number of samples is increased. This highlights the need for more enhanced training methods for quantum models, however, this does not affect the potential of our model to have quantum advantage in sampling the learned probability distribution, since these classical methods are known to be unscalable.

[1] I. H. Sarker, “Machine learning: Algorithms, real-world applications and research directions,” *SN Computer Science*, vol. 2, no. 3, p. 160, 2021.

[2] S. Bond-Taylor, A. Leach, Y. Long, and C. G. Willcocks, “Deep generative modelling: A comparative review of VAEs, GANs, normalizing flows, energy-based and autoregressive models,” *IEEE transactions on pattern analysis and machine intelligence*, 2021.

[3] J. Biamonte, P. Wittek, N. Pancotti, P. Rebentrost, N. Wiebe, and S. Lloyd, “Quantum machine learning,” *Nature*, vol. 549, no. 7671, pp. 195–202, 2017.

[4] M. Schuld, I. Sinayskiy, and F. Petruccione, “The quest for a quantum neural network,” *Quantum Information Processing*, vol. 13, pp. 2567–2586, 2014.

[5] B. M. Terhal and D. P. DiVincenzo, “Adaptive quantum computation, constant depth quantum circuits and arthur-merlin games,” *Quantum Info. Comput.*, vol. 4, no. 2, pp. 134–145, 2004.

[6] S. Aaronson and A. Arkhipov, “The computational complexity of linear optics,” in *Proceedings of the forty-third annual ACM symposium on Theory of computing*, pp. 333–342, 2011.

[7] E. Farhi and A. W. Harrow, “Quantum supremacy through the quantum approximate optimization algorithm,” *arXiv preprint arXiv:1602.07674*, 2016.

[8] F. Arute, K. Arya, R. Babbush, D. Bacon, J. C. Bardin, R. Barends, R. Biswas, S. Boixo, F. G. Brandao, D. A. Buell, *et al.*, “Quantum supremacy using a programmable superconducting processor,” *Nature*, vol. 574, no. 7779, pp. 505–510, 2019.

[9] L. S. Madsen, F. Laudenbach, M. F. Askarani, F. Rortais, T. Vincent, J. F. Bulmer, F. M. Miatto, L. Neuhaus, L. G. Helt, M. J. Collins, *et al.*, “Quantum computational advantage with a programmable photonic processor,” *Nature*, vol. 606, no. 7912, pp. 75–81, 2022.

[10] J. Tian, X. Sun, Y. Du, S. Zhao, Q. Liu, K. Zhang, W. Yi, W. Huang, C. Wang, X. Wu, *et al.*, “Recent advances for quantum neural networks in generative learning,” *IEEE Transactions on Pattern Analysis and Machine Intelligence*, 2023.

[11] M. Benedetti, D. Garcia-Pintos, O. Perdomo, V. Leyton-Ortega, Y. Nam, and A. Perdomo-Ortiz, “A generative modeling approach for benchmarking and training shallow quantum circuits,” *npj Quantum Information*, vol. 5, no. 1, p. 45, 2019.

[12] J.-G. Liu and L. Wang, “Differentiable learning of quantum circuit Born machines,” *Physical Review A*, vol. 98, no. 6, p. 062324, 2018.

[13] B. Coyle, D. Mills, V. Danos, and E. Kashefi, “The Born supremacy: quantum advantage and training of an Ising Born machine,” *npj Quantum Information*, vol. 6, no. 1, p. 60, 2020.

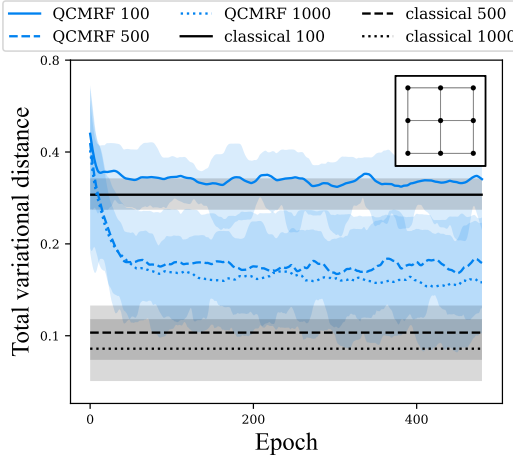


FIG. 12. **Benchmark results against classical BNs.** We consider training sets of size 100, 500 and 1000 for both the classical and quantum models. The QCMRF models are trained with the MMD loss function. The TV distance is computed exactly in each case.

- [14] S. Lloyd and C. Weedbrook, “Quantum generative adversarial learning,” *Physical review letters*, vol. 121, no. 4, p. 040502, 2018.
- [15] P.-L. Dallaire-Demers and N. Killoran, “Quantum generative adversarial networks,” *Physical Review A*, vol. 98, no. 1, p. 012324, 2018.
- [16] M. H. Amin, E. Andriyash, J. Rolfe, B. Kulchytskyy, and R. Melko, “Quantum Boltzmann machine,” *Physical Review X*, vol. 8, no. 2, p. 021050, 2018.
- [17] C. Zoufal, A. Lucchi, and S. Woerner, “Variational quantum Boltzmann machines,” *Quantum Machine Intelligence*, vol. 3, pp. 1–15, 2021.
- [18] J. R. McClean, S. Boixo, V. N. Smelyanskiy, R. Babbush, and H. Neven, “Barren plateaus in quantum neural network training landscapes,” *Nature communications*, vol. 9, no. 1, p. 4812, 2018.
- [19] Z. Holmes, K. Sharma, M. Cerezo, and P. J. Coles, “Connecting Ansatz expressibility to gradient magnitudes and barren plateaus,” *PRX Quantum*, vol. 3, no. 1, p. 010313, 2022.
- [20] M. Ragone, B. N. Bakalov, F. Sauvage, A. F. Kemper, C. Ortiz Marrero, M. Larocca, and M. Cerezo, “A lie algebraic theory of barren plateaus for deep parameterized quantum circuits,” *Nature Communications*, vol. 15, no. 1, p. 7172, 2024.
- [21] E. Fontana, D. Herman, S. Chakrabarti, N. Kumar, R. Yalovetzky, J. Heredge, S. H. Sureshbabu, and M. Pistotia, “Characterizing barren plateaus in quantum ansätze with the adjoint representation,” *Nature Communications*, vol. 15, no. 1, p. 7171, 2024.
- [22] E. R. Anschuetz and B. T. Kiani, “Quantum variational algorithms are swamped with traps,” *Nature Communications*, vol. 13, no. 1, p. 7760, 2022.
- [23] Y.-C. Ho and D. L. Pepyne, “Simple explanation of the no-free-lunch theorem and its implications,” *Journal of optimization theory and applications*, vol. 115, pp. 549–570, 2002.
- [24] K. Poland, K. Beer, and T. J. Osborne, “No free

lunch for quantum machine learning,” *arXiv preprint arXiv:2003.14103*, 2020.

- [25] K. Sharma, M. Cerezo, Z. Holmes, L. Cincio, A. Sornborger, and P. J. Coles, “Reformulation of the no-free-lunch theorem for entangled datasets,” *Physical Review Letters*, vol. 128, no. 7, p. 070501, 2022.
- [26] M. Larocca, F. Sauvage, F. M. Sbahi, G. Verdon, P. J. Coles, and M. Cerezo, “Group-invariant quantum machine learning,” *PRX Quantum*, vol. 3, no. 3, p. 030341, 2022.
- [27] J. J. Meyer, M. Mularski, E. Gil-Fuster, A. A. Mele, F. Arzani, A. Wilms, and J. Eisert, “Exploiting symmetry in variational quantum machine learning,” *PRX Quantum*, vol. 4, no. 1, p. 010328, 2023.
- [28] H. Zheng, Z. Li, J. Liu, S. Strelchuk, and R. Konidor, “Speeding up learning quantum states through group equivariant convolutional quantum ansätze,” *PRX Quantum*, vol. 4, no. 2, p. 020327, 2023.
- [29] J. Bowles, V. J. Wright, M. Farkas, N. Killoran, and M. Schuld, “Contextuality and inductive bias in quantum machine learning,” *arXiv preprint arXiv:2302.01365*, 2023.
- [30] Y. Ding, Y. Ban, M. Sanz, J. D. Martín-Guerrero, and X. Chen, “Quantum active learning,” *arXiv preprint arXiv:2405.18230*, 2024.
- [31] D. Koller and N. Friedman, *Probabilistic graphical models: principles and techniques*. MIT press, 2009.
- [32] D. Heckerman, A. Mamdani, and M. P. Wellman, “Real-world applications of Bayesian networks,” *Communications of the ACM*, vol. 38, no. 3, pp. 24–26, 1995.
- [33] K. P. Murphy, *Machine learning: a probabilistic perspective*. MIT press, 2012.
- [34] G. H. Low, T. J. Yoder, and I. L. Chuang, “Quantum inference on Bayesian networks,” *Physical Review A*, vol. 89, no. 6, p. 062315, 2014.
- [35] S. E. Borujeni, S. Nannapaneni, N. H. Nguyen, E. C. Behrman, and J. E. Steck, “Quantum circuit representation of Bayesian networks,” *Expert Systems with Applications*, vol. 176, p. 114768, 2021.
- [36] X. Gao, E. R. Anschuetz, S.-T. Wang, J. I. Cirac, and M. D. Lukin, “Enhancing generative models via quantum correlations,” *Physical Review X*, vol. 12, no. 2, p. 021037, 2022.
- [37] E. Farhi, J. Goldstone, and S. Gutmann, “A quantum approximate optimization algorithm,” *arXiv preprint arXiv:1411.4028*, 2014.
- [38] H. Krovi, “Average-case hardness of estimating probabilities of random quantum circuits with a linear scaling in the error exponent,” *arXiv preprint arXiv:2206.05642*, 2022.
- [39] L. Von Rueden, S. Mayer, K. Beckh, B. Georgiev, S. Gieselbach, R. Heese, B. Kirsch, J. Pfrommer, A. Pick, R. Ramamurthy, *et al.*, “Informed machine learning—a taxonomy and survey of integrating prior knowledge into learning systems,” *IEEE Transactions on Knowledge and Data Engineering*, vol. 35, no. 1, pp. 614–633, 2021.
- [40] Y. Song and D. P. Kingma, “How to train your energy-based models,” *arXiv preprint arXiv:2101.03288*, 2021.
- [41] V. Gogate, W. Webb, and P. Domingos, “Learning efficient Markov networks,” *Advances in neural information processing systems*, vol. 23, 2010.
- [42] D. Roth, “On the hardness of approximate reasoning,” *Artificial Intelligence*, vol. 82, no. 1-2, pp. 273–302, 1996.
- [43] M. S. Rudolph, S. Lerch, S. Thanasislp, O. Kiss, O. Shaya,

S. Vallecorsa, M. Grossi, and Z. Holmes, “Trainability barriers and opportunities in quantum generative modeling,” *npj Quantum Information*, vol. 10, no. 1, p. 116, 2024.

[44] B. Coyle, M. Henderson, J. C. J. Le, N. Kumar, M. Paini, and E. Kashefi, “Quantum versus classical generative modelling in finance,” *Quantum Science and Technology*, vol. 6, no. 2, p. 024013, 2021.

[45] C. Chow and C. Liu, “Approximating discrete probability distributions with dependence trees,” *IEEE transactions on Information Theory*, vol. 14, no. 3, pp. 462–467, 1968.

[46] M. Benedetti, B. Coyle, M. Fiorentini, M. Lubasch, and M. Rosenkranz, “Variational inference with a quantum computer,” *Physical Review Applied*, vol. 16, no. 4, p. 044057, 2021.

[47] V. Bergholm, J. J. Vartiainen, M. Möttönen, and M. M. Salomaa, “Quantum circuits with uniformly controlled one-qubit gates,” *Phys. Rev. A*, vol. 71, p. 052330, May 2005.

[48] N. Piatkowski and C. Zoufal, “Quantum circuits for discrete graphical models,” *Quantum Machine Intelligence*, vol. 6, no. 2, p. 37, 2024.

[49] A. Gilyén, Y. Su, G. H. Low, and N. Wiebe, “Quantum singular value transformation and beyond: exponential improvements for quantum matrix arithmetics,” in *Proceedings of the 51st Annual ACM SIGACT Symposium on Theory of Computing*, pp. 193–204, 2019.

[50] F. J. Kiwit, M. Marso, P. Ross, C. A. Riofrío, J. Klepsch, and A. Luckow, “Application-oriented benchmarking of quantum generative learning using QUARK,” in *2023 IEEE International Conference on Quantum Computing and Engineering (QCE)*, vol. 1, pp. 475–484, IEEE, 2023.

[51] V. Bergholm, J. Izaac, M. Schuld, C. Gogolin, S. Ahmed, V. Ajith, M. S. Alam, G. Alonso-Linaje, B. Akash-Narayanan, A. Asadi, *et al.*, “Pennylane: Automatic differentiation of hybrid quantum-classical computations,” *arXiv preprint arXiv:1811.04968*, 2018.

[52] D. P. Kingma and J. Ba, “Adam: A method for stochastic optimization,” *arXiv preprint arXiv:1412.6980*, 2014.

[53] A. Arrasmith, Z. Holmes, M. Cerezo, and P. J. Coles, “Equivalence of quantum barren plateaus to cost concentration and narrow gorges,” *Quantum Science and Technology*, vol. 7, no. 4, p. 045015, 2022.

[54] Q. Miao and T. Barthel, “Equivalence of cost concentration and gradient vanishing for quantum circuits: an elementary proof in the riemannian formulation,” *Quantum Science and Technology*, vol. 9, no. 4, p. 045039, 2024.

[55] E. Y. Zhu, S. Johri, D. Bacon, M. Esencan, J. Kim, M. Muir, N. Murgai, J. Nguyen, N. Pisenti, A. Schouela, *et al.*, “Generative quantum learning of joint probability distribution functions,” *Physical Review Research*, vol. 4, no. 4, p. 043092, 2022.

[56] M. J. Bremner, R. Jozsa, and D. J. Shepherd, “Classical simulation of commuting quantum computations implies collapse of the polynomial hierarchy,” *Proceedings of the Royal Society A: Mathematical, Physical and Engineering Sciences*, vol. 467, no. 2126, pp. 459–472, 2011.

[57] A. M. Dalzell, A. W. Harrow, D. E. Koh, and R. L. La Placa, “How many qubits are needed for quantum computational supremacy?,” *Quantum*, vol. 4, p. 264, 2020.

[58] K. Gili, M. Hibat-Allah, M. Mauri, C. Ballance, and A. Perdomo-Ortiz, “Do quantum circuit Born machines generalize?,” *Quantum Science and Technology*, vol. 8, no. 3, p. 035021, 2023.

[59] F. Schlüter, “A survey on independence-based markov networks learning,” *Artificial Intelligence Review*, vol. 42, no. 4, pp. 1069–1093, 2014.

[60] P. Clifford and J. Hammersley, “Markov fields on finite graphs and lattices,” 1971.

[61] A. Glos, A. Krawiec, and Z. Zimborás, “Space-efficient binary optimization for variational quantum computing,” *npj Quantum Information*, vol. 8, no. 1, p. 39, 2022.

[62] B. Bakó, A. Glos, Ö. Salehi, and Z. Zimborás, “Prog-qaoa: Framework for resource-efficient quantum optimization through classical programs,” *Quantum*, vol. 9, p. 1663, 2025.

[63] A. J. Da Silva and D. K. Park, “Linear-depth quantum circuits for multiqubit controlled gates,” *Physical Review A*, vol. 106, no. 4, p. 042602, 2022.

[64] Qiskit contributors, “Qiskit: An open-source framework for quantum computing,” 2023.

[65] C. Manning and H. Schütze, *Foundations of statistical natural language processing*. MIT press, 1999.

[66] A. Ankan and J. Textor, “pgmpy: A python toolkit for bayesian networks,” *Journal of Machine Learning Research*, vol. 25, no. 265, pp. 1–8, 2024.